Linear stability of buffer layer streaks in turbulent channels with variable density and viscosity

Rinaldi, Enrico; Patel, Ashish; Schlatter, Philipp; Pecnik, Rene

DOI
10.1103/PhysRevFluids.2.113903

Publication date
2017

Document Version
Final published version

Published in
Physical Review Fluids

Linear stability of buffer layer streaks in turbulent channels with variable density and viscosity

Enrico Rinaldi,[1,*] Ashish Patel,[2,†] Philipp Schlatter,[1,3,‡] and Rene Pecnik[2,§]
[1]*Department of Mechanics, Linné FLOW Centre, KTH Mechanics, Royal Institute of Technology, SE-100 44 Stockholm, Sweden*
[2]*Process and Energy Department, Delft University of Technology, Leeghwaterstraat 39, 2628 CB Delft, The Netherlands*
[3]*Swedish e-Science Research Centre (SeRC), Stockholm, Sweden*
(Received 21 July 2017; published 15 November 2017)

We investigate the stability of streaks in the buffer layer of turbulent channel flows with temperature-dependent density and viscosity by means of linear theory. The adopted framework consists of an extended set of the Orr-Sommerfeld-Squire equations that accounts for density and viscosity nonuniformity in the direction normal to the walls. The base flow profiles for density, viscosity, and velocity are averaged from direct numerical simulations (DNSs) of fully developed turbulent channel flows. We find that the inner scaling based on semilocal quantities provides an effective parametrization of the effect of variable properties on the linearized flow. The spanwise spacing of optimal buffer layer streaks scales to $\lambda^{\star}_{z,\mathrm{opt}} \approx 90$ for all cases considered and the maximum energy amplification decreases, compared to the one for a flow with constant properties, if the semilocal Reynolds number $\mathrm{Re}^{\star}_{\tau}$ increases away from the walls, consistently with less energetic streaks observed in DNSs of turbulent channels. A secondary stability analysis of the two-dimensional velocity profile formed by the mean turbulent velocity and the nonlinearly saturated optimal streaks predicts a streamwise instability mode with wavelength $\lambda^{\star}_{x,\mathrm{cr}} \approx 230$ in semilocal units, regardless of the fluid property distribution across the channel. The threshold for the onset of the secondary instability is reduced, compared to a constant property flow, if $\mathrm{Re}^{\star}_{\tau}$ increases away from the walls, which explains the more intense ejection events reported in DNSs. The opposite behavior is predicted by the linear theory for decreasing $\mathrm{Re}^{\star}_{\tau}$, in accord with DNS observations. We finally show that the phase velocity of the critical mode of secondary instability agrees well with the convection velocity calculated by DNSs in the near-wall region for both constant and variable viscosity flows.

DOI: 10.1103/PhysRevFluids.2.113903

I. INTRODUCTION

Streamwise velocity streaks are fundamental flow structures in wall bounded shear flows. They play a key role in subcritical transition, where their instability leads to a breakup and to the eventual onset of turbulent motions [1]. Streaks are also important in the fully turbulent regime, where their instability mechanism is crucial to sustain the near-wall regeneration cycle [2,3]. The latter can be subdivided into three main steps, namely, (i) the formation of streamwise low- and high-speed streaks, (ii) the streaks' instability and breakup, and (iii) the formation of quasistreamwise vortices responsible for generating new streaks. The first two processes are predominantly linear mechanisms;

*erinaldi@mech.kth.se
†a.patel@tudelft.nl
‡pschlatt@mech.kth.se
§r.pecnik@tudelft.nl

the generation and amplification of streaks occurs by means of the lift-up effect [4] and the streaks' streamwise instability is triggered by a linearly unstable mode.

The linearized Navier-Stokes equations have been proven in the past to provide an effective framework to study the characteristics of streaks in turbulent flows. The operator resulting from the linearization around a mean turbulent velocity profile, which is linearly stable, is non-normal, hence it supports transient amplification of perturbations in a similar fashion to what is predicted for stable laminar base flows [5–7]. Butler and Farrell [8] showed that the optimization of the energy growth function constrained to a characteristic turbulent time scale yields to optimal flow structures that are streamwise-independent streaks. Their spanwise spacing in viscous wall units is $\lambda_z^+ \approx 100$, in close analogy to the streak spacing observed in experiments [9]. del Álamo and Jiménez [10], and subsequently Pujals *et al.* [11], introduced in the Orr-Sommerfeld-Squire equations a spatially dependent effective viscosity coefficient that accounts for the contribution of the molecular viscosity of the fluid (constant) and of the eddy viscosity [variable in the wall-normal direction (see [12,13])], in which the nonlinearity of the turbulent flow is lumped. Their unconstrained linear growth analysis resulted in two optimal streaks, as opposed to the single optimal observed for laminar flows and in Ref. [8]. The two optimal wavelengths correspond to (i) large structures in the crossflow plane spaced by $\lambda_z = 4h$, with h the half-channel height, for which the maximum energy growth $G_{\max}$ increases with the Reynolds number, and (ii) small-scale buffer layer streaks spaced by $\lambda_z^+ = 92$, with $G_{\max} \approx 2.6$, which does not depend on the Reynolds number. A larger maximum growth can be achieved in the case in which the energy norm adopted in the optimization is not calculated across the whole domain, as in the referenced works, but is constrained to the near-wall region [14].

Linearized equations were used by Schoppa and Hussain [15] to investigate the secondary instability of streaks in turbulent channels and to calculate their critical amplitude. They found that only 20% of the streaks simulated in direct numerical simulations (DNSs) meet the instability threshold calculated from linear theory, thus highlighting the limitations of using the normal mode instability to explain the vortex regeneration mechanism. Nevertheless, linear theory can be invoked to describe, at least partly, the dynamics of bursting events. Jiménez [16] argued that an Orr-like transient process is responsible for the amplification of the disturbance energy generated by the streaks' breakdown in turbulent channels and subsequently demonstrated that linearized models can predict strong bursts of the large scales in up to 70% of the total time [17]. Large-scale structures in the crossflow plane were investigated by Cossu *et al.* [18] and by Park *et al.* [19], who found larger critical thresholds for secondary instabilities with respect to the laminar case. Alizard [20] studied streaks in the logarithmic region and found that the size of the crossflow structures is proportional to the wall distance, which is in agreement with the attached eddy hypothesis [21]. Turbulent channel flows with adverse pressure gradients were studied by Marquillie *et al.* [22] and an extension to compressible flows was presented by Alizard *et al.* [23]. A linear model was successfully used to explain large-scale recurrent burst in rotating turbulent channel flows in cases where the predicted unstable wave is not altered excessively by the surrounding turbulence [24,25].

While the majority of the literature is concerned with turbulent flows of constant property fluids, variable property flows play a relevant role in many engineering applications. The fluid temperature can be nonuniform as the result of heat transfer or compressibility effects in high-speed flows. As a consequence, fluid properties such as density and viscosity are also nonuniform and directly affect turbulence as they appear in the equations governing the fluid motion. Most of the research on turbulence with near-wall property gradients has been performed for heated or cooled high-speed compressible flows. Several researchers observed a modulation of the spatial structure of streaks, which become more elongated in a supersonic channel flow with cold isothermal walls [26–28], while the opposite effect was documented in the case of heated walls in the same flow configuration [28]. The modified spatial coherence of streaks disappears if semilocal units are used [29,30], despite a modulating effect of variable properties remaining on turbulence statistics and flow anisotropy [31]. Recently, Patel *et al.* [32] provided rigorous mathematical support for the semilocal scaling and showed that the dominating parameter in characterizing fluid flows with different property

distributions is the semilocal Reynolds number

$$\mathrm{Re}_\tau^\star = \frac{\sqrt{\overline{\rho}/\rho_w}}{\overline{\mu}/\mu_w}\mathrm{Re}_\tau, \tag{1}$$

with the overbar indicating Reynolds averages and the subscript w averaged wall properties. Here $\mathrm{Re}_\tau = \rho_w h u_\tau/\mu_w$ is the Reynolds number based on the friction velocity $u_\tau = \sqrt{\tau_w/\rho_w}$. Flows with similar $\mathrm{Re}_\tau^\star$ distributions exhibit similar statistics and turbulence features, irrespective of individual density or viscosity profiles. For cases where $\mathrm{Re}_\tau^\star$ decreases away from the walls, streaks in the buffer layer are strengthened and ejection events linked to their instability are less intense. The opposite occurs for increasing $\mathrm{Re}_\tau^\star$. Gradients in $\mathrm{Re}_\tau^\star$ influence the van Driest transformed mean velocity profiles, which affects the inclination and tilting angles of the streamwise vortices, thus providing a physical interpretation for the above-mentioned turbulence modulations [33].

In this paper we address the modulating effect of variable density and viscosity on buffer layer streaks within the linearized Navier-Stokes framework. We use a modified set of Orr-Sommerfeld-Squire equations that includes nonuniform density and viscosity profiles in the direction normal to the walls, which are extracted from DNSs from Ref. [32]. We seek a theoretical justification for previous observations of strengthening and stabilization of streaks in the case of decreasing semilocal Reynolds number away from the walls (the effect is opposite if $\mathrm{Re}_\tau^\star$ increases). Furthermore, we want to assess whether the effectiveness of the semilocal scaling in parametrizing the effect of variable properties additionally applies to the geometrical characteristics of calculated linear optimal structures and their secondary instability mode.

The paper is structured as follows. The data set used and the most important features of the considered variable property flows are discussed in Sec. II. In Sec. III we present the procedure adopted to define the base flow conditions for the linearization starting from the DNS data. A linear growth analysis of the mean turbulent profiles is performed in Sec. IV and the secondary stability of the calculated optimal streaks is investigated in Sec. V. A summary and conclusions are presented in Sec. VI.

II. TURBULENT FLOW CONFIGURATIONS

The turbulent flow cases studied in this paper are taken from Ref. [32], where DNSs of the low-Mach-number approximation of the Navier-Stokes equations are performed using different constitutive relations for density and viscosity as a function of temperature. The flow is driven by a constant pressure gradient in channels with isothermal walls and heated by a constant volumetric heat source. The latter results in symmetric averaged temperature profiles in the direction normal to the walls, whose maximum value is located at the centerline y_c. All simulations are performed at the same Reynolds number based on the friction velocity at the walls, namely, $\mathrm{Re}_\tau = 395$. The reader is referred to the original paper for further details on the flow configuration, the numerical scheme, and its validation.

The considered cases and the respective flow conditions are summarized in Table I. The constitutive relations of density and viscosity as functions of temperature are given in columns 2 and 3, respectively. Depending on those, $\mathrm{Re}_\tau^\star$ remains constant, decreases, or increases along the half-channel height and is representative of the qualitative behavior of a constant property fluid, a gas, or a liquid that is cooled from the walls. The last column gives the value of the semilocal Reynolds number at the channel center, $h^\star = \mathrm{Re}_\tau^\star(y_c)$. Other transport properties, i.e., thermal conductivity and specific heat, are constant in all simulations. Figure 1 displays $\mathrm{Re}_\tau^\star$ across the half-channel height for each flow case studied and Fig. 2 depicts the corresponding distributions of averaged density and viscosity. The cases are grouped into four pairs of similar $\mathrm{Re}_\tau^\star$ distributions. The first pair consists of a constant property case CP and a variable property case C$\mathrm{Re}_\tau^\star$, for which $\mathrm{Re}_\tau^\star$ is constant across the channel. The second pair is characterized by a $\mathrm{Re}_\tau^\star$ that decreases away from the walls and consists of case GL, which exhibits gaslike property variations, and case S$\mathrm{Re}_\tau^\star$GL, for which only viscosity is a function of temperature and density is constant. The third pair consists of a variable

TABLE I. Flow cases studied, taken from Ref. [32]: constant property case (CP), constant $\mathrm{Re}_\tau^\star$ case ($\mathrm{CRe}_\tau^\star$), case with gaslike property variations (GL) and with similar distribution of semilocal Reynolds number ($\mathrm{SRe}_\tau^\star$GL), case with constant kinematic viscosity (C_ν) and with similar distribution of semilocal Reynolds number ($\mathrm{SRe}_\tau^\star\mathrm{C}_\nu$), and case with liquidlike property variations (LL) and with similar distribution of semilocal Reynolds number ($\mathrm{SRe}_\tau^\star$LL). The semilocal Reynolds number at the centerline is indicated by $h^\star = \mathrm{Re}_\tau^\star(y_c)$. For all cases $\mathrm{Re}_\tau = \mathrm{Re}_{\tau,w}^\star = 395$.

Case	ρ/ρ_w	μ/μ_w	$h^\star$
CP	1	1	395
$\mathrm{CRe}_\tau^\star$	$(T/T_w)^{-1}$	$(T/T_w)^{-0.5}$	395
GL	$(T/T_w)^{-1}$	$(T/T_w)^{0.7}$	142
$\mathrm{SRe}_\tau^\star$GL	1	$(T/T_w)^{1.2}$	152
C_ν	$(T/T_w)^{-1}$	$(T/T_w)^{-1}$	538
$\mathrm{SRe}_\tau^\star\mathrm{C}_\nu$	1	$(T/T_w)^{-0.5}$	532
LL	1	$(T/T_w)^{-1}$	703
$\mathrm{SRe}_\tau^\star$LL	$(T/T_w)^{-1}$	$(T/T_w)^{-1.5}$	719

property case with constant kinematic viscosity C_ν that results in an increase of $\mathrm{Re}_\tau^\star$ away from the walls and of case $\mathrm{SRe}_\tau^\star\mathrm{C}_\nu$, which has constant density but variable viscosity. For the fourth pair $\mathrm{Re}_\tau^\star$ increases with a stronger gradient away from the wall. This pair consists of case LL, which exhibits liquidlike property variations, and case $\mathrm{SRe}_\tau^\star$LL, for which both density and viscosity are functions of temperature.

A detailed discussion of the modulating effect of flow properties on turbulence characteristics and of the effectiveness of semilocal scaling in characterizing variable property flows is presented in Refs. [32,33] and will not be repeated here for the sake of brevity. Our present discussion is limited to the main conclusions of the referenced papers, which serve as a motivation for this work. Flow structures in turbulent flows with variable properties show similar spatial characteristics if semilocal scaling is adopted, i.e., if the local value of $\mathrm{Re}_\tau^\star$ is used instead of Re_τ. Semilocal coordinates are defined as $x_i^\star = (x_i/h)\mathrm{Re}_\tau^\star$, in analogy with the standard definition of viscous units $x_i^+ = (x_i/h)\mathrm{Re}_\tau$. Here $x_i = (x, y, z)$ indicate the streamwise, wall-normal, and spanwise directions. Semilocal scaling

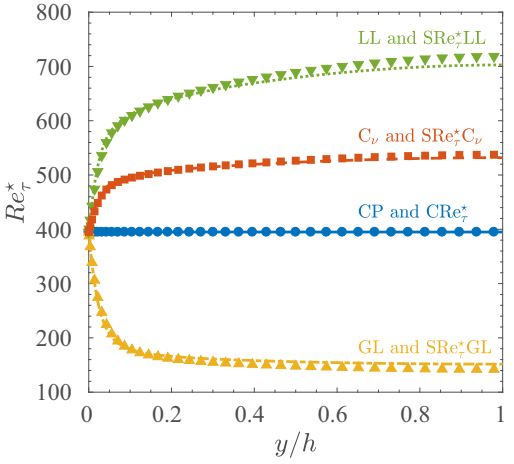

FIG. 1. Distribution of the semilocal Reynolds number $\mathrm{Re}_\tau^\star$ for the flow cases of Table I. Lines indicate constant density flows and symbols are ◯, $\mathrm{CRe}_\tau^\star$; □, C_ν; △, GL; and ▽, $\mathrm{SRe}_\tau^\star$LL. The wall is located at $y/h = 0$ and the centerline at $y/h = 1$. Only the half channel is shown.

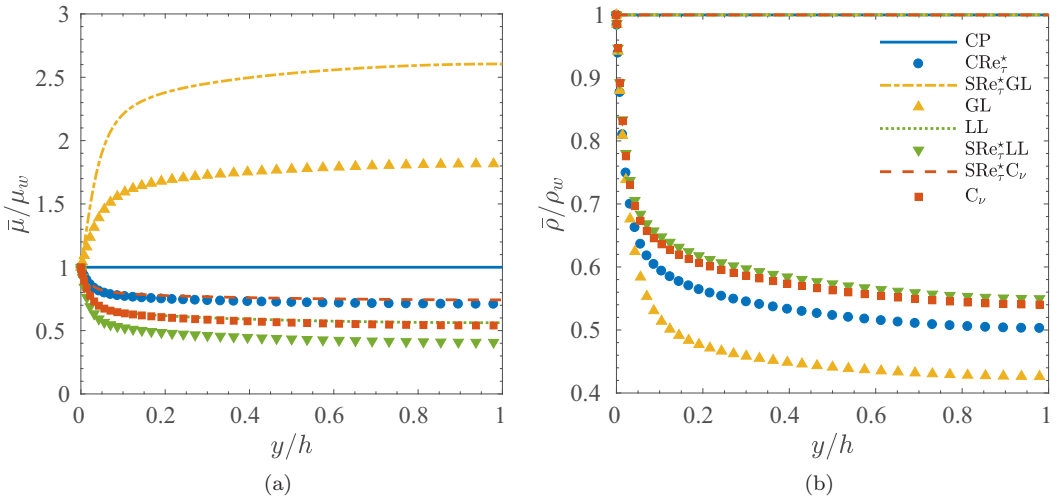

FIG. 2. Reynolds-averaged distributions of (a) viscosity and (b) density for the flow cases of Table I. The wall is located at $y/h = 0$ and the centerline at $y/h = 1$. Only the half channel is shown.

is able to account for some of the differences seen between variable and constant property flows and to provide a universal scaling law for the turbulent mean profile [33,34], however this does not extend to higher-order turbulent statistics. The reason is a modification of near-wall vortical structures by gradients of $\mathrm{Re}^\star_\tau$. Flows with different property distributions but similar $\mathrm{Re}^\star_\tau$ profiles display similar turbulence characteristics. Relevant for the present paper is the modulation of the intensity of buffer layer streaks in flows with $\mathrm{Re}^\star_\tau$ gradients in the near-wall region. Additionally, the streaks' stability is affected, which results in altered ejection events near the walls originated from their burst. In support of this statement we report in Fig. 3 the joint probability density functions (PDFs) of the streamwise and wall-normal velocity fluctuations (denoted by u and v, respectively) with respect to the Favre-averaged velocity profile and the probability-weighted Reynolds shear stress $\rho uv/\tau_w P(\sqrt{\rho}u/\sqrt{\tau_w}, \sqrt{\rho}v/\sqrt{\tau_w})$ for cases CP, GL, and LL at the vertical location $y^\star = 12$. This location is chosen as it corresponds to the peak of turbulent kinetic energy production and therefore indicates where physically relevant phenomena occur. Furthermore, streak spacing in semilocal units is universal above $y^\star \approx 12$ [33]. Contours show that the flow case CRe$^\star_\tau$, for which properties change across the channel in such a way that the semilocal Reynolds number is constant ($\mathrm{Re}^\star_\tau = \mathrm{Re}_\tau$), has the same statistics as the constant property case (CP). On the other hand, ejection events are weaker for the GL case and the intensity of the low-speed streaks strengthens. The opposite occurs for the LL case that corresponds to increasing $\mathrm{Re}^\star_\tau$ away from the walls. In the following sections we will seek a justification for the discussed effect of variable density and viscosity on the streak characteristics using linear theory.

III. BASE FLOW PROFILES

In order to obtain base profiles to be used as reference conditions for the linearization of the Navier-Stokes equations, we perform a piecewise polynomial fitting of mean DNS data. Smoothness of the functions and their derivatives is imposed between adjacent polynomials, whose order is manually adapted to ensure a good approximation of the data in both the near-wall region and centerline of the channel. The knowledge of polynomial coefficients allows us to calculate smooth derivatives of the properties of interest. In contrast to constant property cases, the interpolation procedure is here necessary as no models are available for the mean temperature and eddy viscosity distributions in turbulent channels with variable density and viscosity. Following Refs. [10,11,13], we define an effective viscosity of the reference flow as the sum of the molecular viscosity of the

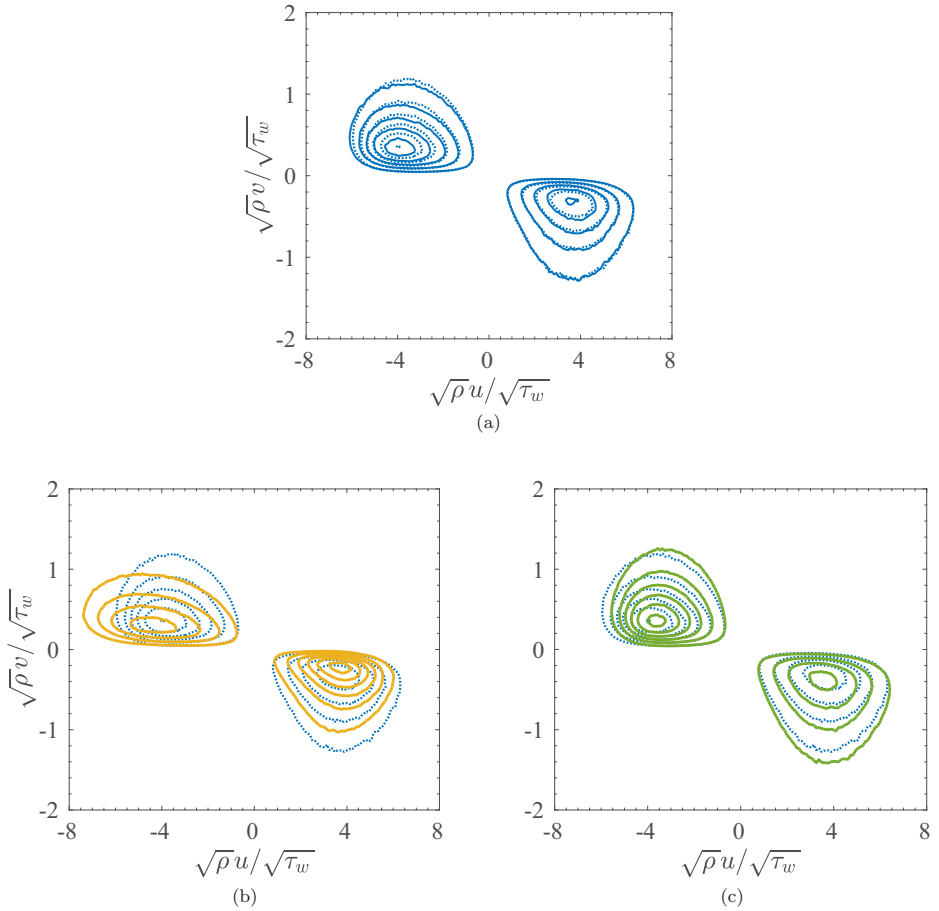

FIG. 3. Joint PDFs of the streamwise and wall-normal Favre-averaged velocity fluctuations. Values are nondimensionalized by the instantaneous density and wall shear stress. Contours indicate the probability-weighted Reynolds shear stress $\rho uv/\tau_w P(\sqrt{\rho}u/\sqrt{\tau_w}, \sqrt{\rho}v/\sqrt{\tau_w})$. Dotted lines refer to case CP in each image; solid lines indicate (a) $\mathrm{CRe}^{\star}_{\tau}$, (b) GL, and (c) LL. For each case displayed, lines are spaced by 0.02 and range from -0.02 (most outer) to -0.12.

fluid and of an eddy viscosity contribution in which the effect of turbulence is lumped

$$\mu_e(y) = \frac{\mu(\overline{T}) + \mu_t(y)}{\mu_w}. \tag{2}$$

The molecular viscosity is calculated using the Reynolds-averaged temperature from DNSs, $\overline{T} = \overline{T}(y)$, and the constitutive relations from Table I. The physical condition $\overline{T}'_w = \phi$ is imposed at the solid walls, in which the prime indicates the derivative with respect to y and ϕ is the volumetric heat source used in the DNS. The interpolated temperature is also used to calculate the reference density, as $\rho = \rho(\overline{T})$, and its derivatives. Note that for a generic thermophysical property $\psi(\overline{T}) \neq \overline{\psi(T)}$. These two values can significantly differ in the case of strong temperature fluctuations or in the case in which the constitutive relation for ψ is highly sensitive to the value of its argument, as is the case for turbulent flows at supercritical pressures [35]. In all flow cases considered here, this inconsistency in fluid property evaluations is limited and does not affect the results and our discussion. The eddy

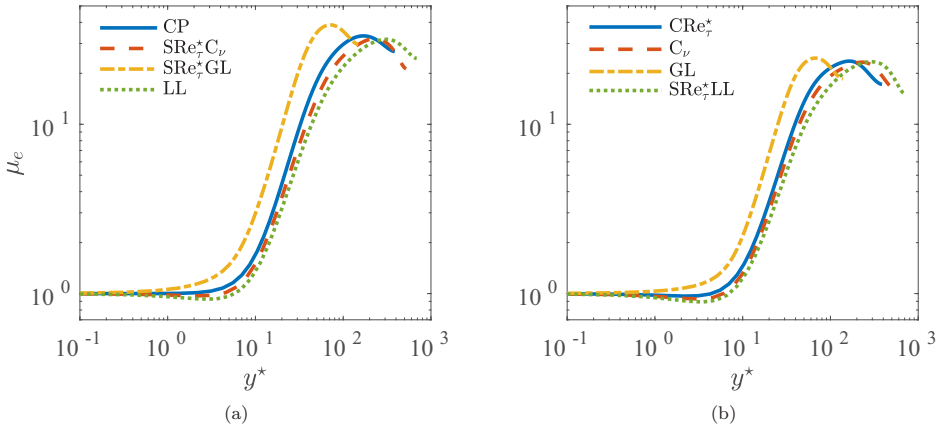

FIG. 4. Effective viscosity profiles $\mu_e = \mu + \mu_t$ interpolated from the data set described in Sec. II and summarized in Table I. Results are organized into (a) constant and (b) temperature-dependent density cases. The molecular viscosity is a function of temperature for both.

viscosity is defined as

$$\mu_t(y) = -\frac{\widetilde{\rho u v}}{dU/dy}, \tag{3}$$

with ρ the instantaneous turbulent density field and the tilde indicating Favre averaging. The physical constraints imposed on the interpolation of the eddy viscosity are

$$\mu_{t,w} = 0, \quad \mu'_{t,w} = 0, \quad \mu''_{t,w} = 0, \tag{4}$$

where the prime replaces d/dy. The resulting effective viscosity profiles for the cases reported in Table I are displayed in Fig. 4. Note that for cases C$_\nu$, SRe$_\tau^\star$C$_\nu$, LL, and SRe$_\tau^\star$LL the effective viscosity falls below the value at the wall due to the predominant contribution of the decreasing molecular viscosity in the viscous sublayer.

The base velocity profile is calculated from the one-dimensional momentum balance in the streamwise direction, which reads

$$\frac{dU^+}{d(y/h)} = -(y/h)\frac{\mathrm{Re}_\tau}{\mu_e}, \tag{5}$$

with $y/h \in [-1,1]$. The effective viscosity coefficient is given by Eq. (2) and the plus superscript indicates normalization by the friction velocity $u_\tau = \sqrt{\tau_w/\rho_w}$. The result is a velocity profile that (i) is consistent with the constitutive relations for the mean flow properties reported in Table I and used to solve the Orr-Sommerfeld-Squire system (10) and (11) and (ii) has smooth derivatives across the channel height. For these reasons, the described approach is preferred over a direct interpolation of DNS data for velocity and its derivatives. The comparison between the base velocity profiles calculated from Eq. (5) and the mean DNS profiles, respectively indicated by lines and symbols, for all cases considered, is reported in Fig. 5 and shows satisfactory agreement. Appreciable deviations are limited to the cases GL and SRe$_\tau^\star$GL only and are located in the center of the channel. Here the eddy viscosity coefficient calculated from the DNS displays large oscillations due to the vanishing denominator in Eq. (3) and its smoothed profile locally deviates from the DNS data. This discrepancy is the reason for the differences observed in Fig. 5. In order to rule out that these affect our results, we have verified that the influence of using a calculated or interpolated base velocity profile is indeed negligible by performing a limited set of calculations using both, which is not reported here.

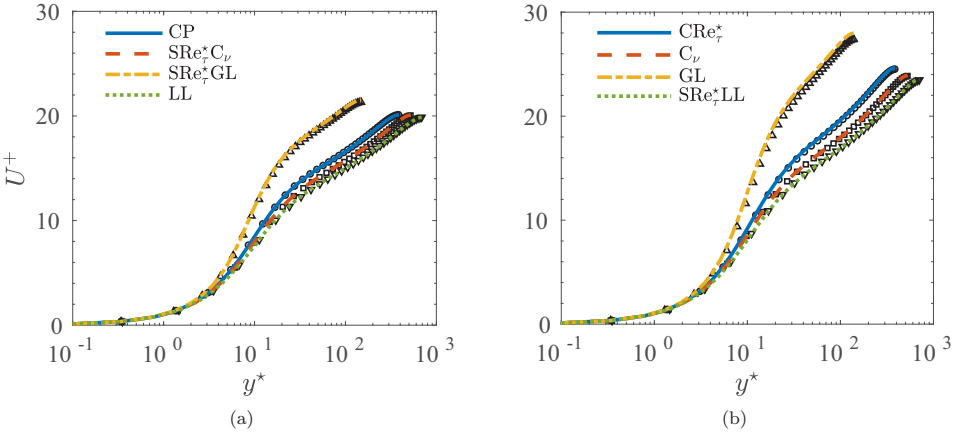

FIG. 5. Base velocity profiles calculated using Eq. (5) and the interpolated viscosity of Fig. 4. Results are organized into (a) constant and (b) temperature-dependent density cases. Mean velocity profiles extracted from DNSs are also reported for comparison and are indicated by symbols that correspond to ◯, CP and $\mathrm{CRe}_\tau^\star$; □, C_ν and $\mathrm{SRe}_\tau^\star \mathrm{C}_\nu$; △, GL and $\mathrm{SRe}_\tau^\star \mathrm{GL}$; and ▽, LL and $\mathrm{SRe}_\tau^\star \mathrm{LL}$.

IV. ALGEBRAIC GROWTH OF OPTIMAL STREAKS

The dynamics of a small-amplitude velocity $\mathbf{u} = (u,v,w)$ and pressure p perturbations to a base flow $\mathbf{U} = (U(y),0,0)$ with nonuniform viscosity and density in the direction normal to the walls, namely, $\mu = \mu(y)$ and $\rho = \rho(y)$, is governed by the linearized Navier-Stokes equations

$$\frac{\partial u}{\partial x} + \frac{\partial v}{\partial y} + \frac{\partial w}{\partial z} = -\frac{\rho'}{\rho} v, \tag{6}$$

$$\rho \frac{\partial u}{\partial t} + \rho U \frac{\partial u}{\partial x} + \rho U' v = -\frac{\partial p}{\partial x} + \frac{1}{\mathrm{Re}_\tau}\left[\mu \nabla^2 u + \mu'\left(\frac{\partial u}{\partial y} + \frac{\partial v}{\partial x}\right) - \frac{1}{3}\frac{\mu\rho'}{\rho}\frac{\partial v}{\partial x}\right], \tag{7}$$

$$\rho \frac{\partial v}{\partial t} + \rho U \frac{\partial v}{\partial x} = -\frac{\partial p}{\partial y} + \frac{1}{\mathrm{Re}_\tau}\left[\mu \nabla^2 v + 2\mu' \frac{\partial v}{\partial y} - \frac{1}{3}\frac{\mu\rho''}{\rho} v - \frac{1}{3}\frac{\mu\rho'}{\rho}\frac{\partial v}{\partial y} + \frac{1}{3}\frac{\mu(\rho')^2}{\rho^2} v + \frac{2}{3}\frac{\mu'\rho'}{\rho} v\right], \tag{8}$$

$$\rho \frac{\partial w}{\partial t} + \rho U \frac{\partial w}{\partial x} = -\frac{\partial p}{\partial z} + \frac{1}{\mathrm{Re}_\tau}\left[\mu \nabla^2 w + \mu'\left(\frac{\partial v}{\partial z} + \frac{\partial w}{\partial y}\right) - \frac{1}{3}\frac{\mu\rho'}{\rho}\frac{\partial v}{\partial z}\right]. \tag{9}$$

Quantities are nondimensionalized by the half-channel height h, the friction velocity u_τ, wall density ρ_w, and viscosity μ_w and the $+$ superscript is dropped. Fluctuations of density and viscosity are not accounted for in the present linearized model, i.e., the energy equation is passive and the ρ and μ profiles are frozen. The above system of equations can be recast in the wall-normal velocity v and vorticity η formulation, in which the continuity constraint is automatically satisfied and the pressure does not appear explicitly. This gives extended versions of the Orr-Sommerfeld-Squire equations that read

$$\begin{aligned}
&\frac{\partial}{\partial t}\left(\rho'' + 2\rho'\frac{\partial}{\partial y} + \rho\nabla^2\right)v + \left(\rho U \nabla^2 + \rho'' U + 2\rho' U \frac{\partial}{\partial y} - \rho U''\right)\frac{\partial v}{\partial x} \\
&= \frac{1}{\mathrm{Re}_\tau}\left\{\mu_e \nabla^4 v + 2\mu_e' \nabla^2 \frac{\partial v}{\partial y} + \mu_e''\left[\frac{\partial^2}{\partial y^2} - \left(\frac{\partial^2}{\partial x^2} + \frac{\partial^2}{\partial z^2}\right)\right]v + \mu_e\left(\frac{\partial^2}{\partial x^2} + \frac{\partial^2}{\partial z^2}\right)\frac{\partial}{\partial y}\left(\frac{\rho' v}{\rho}\right)\right. \\
&\left. + \mu_e \frac{\partial^3}{\partial y^3}\left(\frac{\rho' v}{\rho}\right) + 2\mu_e'\left(\frac{\partial^2}{\partial x^2} + \frac{\partial^2}{\partial z^2}\right)\frac{\rho' v}{\rho} + 2\mu_e'\frac{\partial^2}{\partial y^2}\left(\frac{\rho' v}{\rho}\right) + \mu_e''\frac{\partial}{\partial y}\left(\frac{\rho' v}{\rho}\right)\right\},
\end{aligned} \tag{10}$$

$$\rho\frac{\partial\eta}{\partial t}+\rho U\frac{\partial\eta}{\partial x}+\rho U'\frac{\partial v}{\partial z}=\frac{1}{\mathrm{Re}_\tau}\left[\mu_e\nabla^2\eta+\mu_e'\frac{\partial\eta}{\partial y}\right], \tag{11}$$

in which we have replaced the viscosity of the fluid with the effective viscosity defined in Eq. (2). The boundary conditions at the solid walls are

$$v_w=0,\quad v_w'=0,\quad \eta_w=0. \tag{12}$$

In the following, we assume perturbations of the form

$$\mathbf{u}(x,y,z,t)=\hat{\mathbf{u}}(y,t)e^{i\alpha x+i\beta z}, \tag{13}$$

with α and β the streamwise and spanwise wave numbers. Equations (10) and (11) are numerically discretized using a standard approach based on Chebyshev polynomials ($N=151$) collocated on Gauss-Lobatto nodes [1].

Mean turbulent velocity profiles are known to be linearly stable [13], which applies also to the ones reported in Fig. 5. Any given perturbation whose evolution is governed by Eqs. (10) and (11) decays for long enough times. However, the non-normality of the Orr-Sommerfeld-Squire operator transiently amplifies perturbations over short times [1]. We define an optimal growth function as the maximum amplification of perturbation kinetic energy over all possible initial conditions $\hat{\mathbf{u}}_0$,

$$\hat{G}(\alpha,\beta,t)=\max_{\hat{\mathbf{u}}_0}\frac{\|\hat{\mathbf{u}}(t)\|_E^2}{\|\hat{\mathbf{u}}_0\|_E^2}, \tag{14}$$

with $\|\cdot\|_E$ denoting the energy norm [36]. The maximum optimal growth is

$$G_{\max}(\alpha,\beta)=\max_{t>0}\hat{G}(\alpha,\beta,t). \tag{15}$$

Similarly to the laminar case and in accord with previous studies, which used turbulent base velocity profiles (see, e.g., [10,11]), we find that the highest maximum optimal growth is obtained with streamwise-independent ($\alpha=0$) velocity streaks and rolls. Curves of $G_{\max}(0,\beta)$ for the complete set of variable property flows considered here are displayed in Fig. 6. Since the focus of this paper is on buffer layer streaks and on the scaling of the inner peak of $G_{\max}$, we chose to normalize the spanwise wavelength in semilocal units $\lambda_z^\star=2\pi\overline{\mathrm{Re}}_\tau^\star/\beta$, with $\overline{\mathrm{Re}}_\tau^\star=\mathrm{Re}_\tau^\star(y^\star=12)$. The choice of the wall-normal location $y^\star=12$ as reference was discussed in Sec. II. Note that $\lambda^\star\equiv\lambda^+$ for a constant property flow or a flow with a constant semilocal Reynolds-number distribution. The figure also includes results for constant density and viscosity turbulent channels at higher Reynolds numbers $\mathrm{Re}_\tau=550,950$. Numerical data for $\mathrm{Re}_\tau=950$ are taken from the available data set of Hoyas and Jiménez [37]. Results show the typical double-peak structure, i.e., large- and small-scale optimal streaks. The outer layer peaks for the constant property cases show the known dependence on Re_τ (the higher the Re_τ, the higher the peak), while the inner peak is only marginally affected by the Reynolds number [11]. The main results in terms of maximum optimal growth and optimal spanwise wavelength of small-scale streaks are summarized in Table II.

Lines corresponding to cases with similar $\mathrm{Re}_\tau^\star$ profiles collapse at the small scales, up to $\lambda_z^\star\approx 300$, thus extending the effectiveness of the parametrization based on semilocal quantities to the study of turbulent flows with variable properties by means of linear theory. The reason behind the observed behavior is that, as the wave number β increases, $\rho U'\partial v/\partial z$ dominates in Eq. (11). This term represents the coupling between Eqs. (10) and (11) and can be rewritten as $\rho U'\partial v/\partial z=\sqrt{\rho}U'\partial\sqrt{\rho}v/\partial z=U_{\mathrm{vD}}'\partial\sqrt{\rho}v/\partial z$. Here U_{vD} is the mean van Driest velocity, which is similar for flow cases with similar $\mathrm{Re}_\tau^\star$ profiles. The same applies for $\sqrt{\rho}v$, which is consistent with the semilocal scaling for the velocity. The optimal spanwise wavelength of the streaks corresponding to the inner peak of $G_{\max}$ also scales in semilocal units and is approximately constant to $\lambda_{z,\mathrm{opt}}^\star\approx 80$–$93$ for all cases, regardless of the specific property distributions across the channel. In terms of classical viscous units, the optimal values are scattered on a significantly larger range, $\lambda_{z,\mathrm{opt}}^+\approx 70$–$160$. The

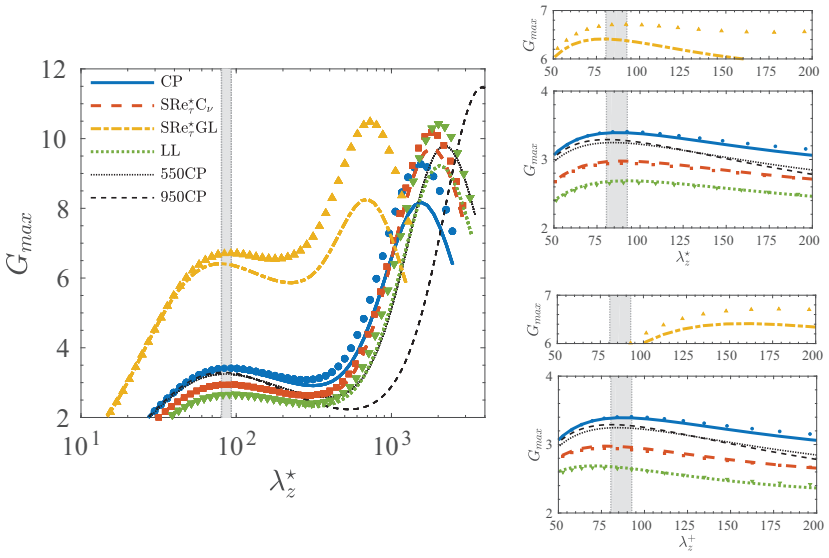

FIG. 6. Maximum optimal growth function for the flow cases of Table I. Results for constant property flow at $\mathrm{Re}_\tau = 550,950$ are also included. Data for $\mathrm{Re}_\tau = 950$ are taken from the available database by Hoyas and Jiménez [37]. Lines and symbols (same as in Fig. 1) correspond to constant and variable density cases, respectively. The spanwise wavelength is scaled in semilocal units as $\lambda^\star_z = 2\pi\overline{\mathrm{Re}}^\star_\tau/\beta$. The shaded area demarcates the range of maximum and minimum values of $\lambda^\star_{z,\mathrm{opt}}$ for the investigated flow cases. Panels on the right magnify the regions near the peaks of $G_{\max}$ and show the difference between semilocal (top two) and classical inner scaling (bottom two).

cases GL and SRe$^\star_\tau$GL display the largest discrepancies in terms of similar $G_{\max}$ profiles at small wavelengths of $\lambda^\star_{z,\mathrm{opt}}$, if compared to the other three pairs of flow cases. This is due to the low semilocal Reynolds number reached at the centerline, $h^\star = 142$ and $h^\star = 152$, respectively, that is at the limit of the applicability of the adopted linearized framework, which was originally proposed for moderate to high friction Reynolds numbers [10,11]. The low values of $h^\star$ attained by the cases GL and SRe$^\star_\tau$GL also result in a scale separation that is not as large as for the other cases considered. The consequence is that the inner peak of $G_{\max}$ can emerge only on a limited range of scales (or wave numbers) and is influenced by the large scales. A linear growth analysis of a constant property flow at $\mathrm{Re}_\tau = 150$ using the customary eddy viscosity model of Cess [12] (see, e.g., [10,11,13]) does

TABLE II. Characteristics of the inner peak of the maximum optimal growth functions in Fig. 6.

Case	$G_{\max}$	β_{opt}	$\lambda^\star_{z,\mathrm{opt}}$	$\lambda^+_{z,\mathrm{opt}}$
CP	3.393	28.41	87.36	87.36
CRe$^\star_\tau$	3.388	28.03	88.56	88.56
550CP	3.247	41.02	84.24	84.24
950CP	3.308	74.17	80.48	80.48
C$_\nu$	2.936	32.74	87.41	75.79
SRe$^\star_\tau$C$_\nu$	2.977	31.77	90.85	78.13
LL	2.689	35.30	92.60	70.31
SRe$^\star_\tau$LL	2.655	34.76	92.44	71.40
GL	6.582	15.21	81.54	158.00
SRe$^\star_\tau$GL	6.413	15.71	81.39	163.18

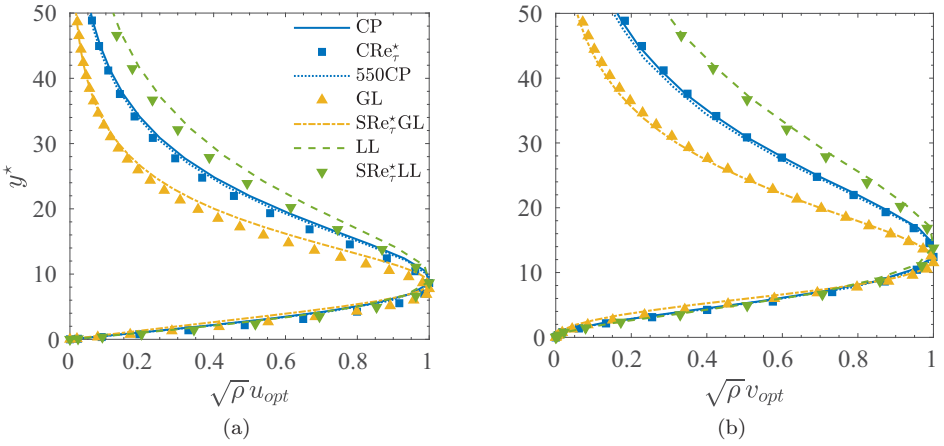

FIG. 7. Optimal initial velocity profiles calculated for $\lambda^\star_{z,\mathrm{opt}}$. Profiles are normalized by their peak values.

not show the inner peak of $G_{\max}$ at all (not shown here) due to the low value of the eddy viscosity. The fact that $\mathrm{Re}^\star_\tau$ approaches 140–150 only in the central part of the domain is the reason why a "turbulent" effect, which manifests itself in terms of an inner peak of $G_{\max}$, is still visible near the walls, however not entirely distinct from the the peak at $\lambda_z = 4h$.

A further remarkable feature of the results in Fig. 6 and Table II is that variable flows with $\mathrm{Re}^\star_\tau$ gradients modulate the maximum optimal growth of the small-scale streaks, which does not depend on Re_τ for constant property flows. While $G_{\max}(0,\lambda^\star_{z,\mathrm{opt}})$ for the case CRe$^\star_\tau$ is similar to the value for a constant property flow, $G_{\max}(0,\lambda^\star_{z,\mathrm{opt}})$ decreases if $\mathrm{Re}^\star_\tau$ increases away from the walls and the effect is proportional to the $\mathrm{Re}^\star_\tau$ gradients. The opposite occurs for decreasing $\mathrm{Re}^\star_\tau$. In this case, the significantly higher maximum optimal growth for cases GL and SRe$^\star_\tau$GL is a combination of the variable $\mathrm{Re}^\star_\tau$ and low-Reynolds-number effect. As previously discussed, the small-scale separation prevents the emergence of an inner peak that is independent from the outer one, hence its value is strongly influenced by the optimal growth sustained at the large scales. The qualitative effect inferred from Fig. 6 provides a justification for the strengthening of streaks for gaslike distributions of $\mathrm{Re}^\star_\tau$ and weakening for liquidlike cases previously reported in the literature [32].

The optimal initial streamwise and wall-normal velocity profiles corresponding to the inner peak of the optimal growth function are shown in Fig. 7. Results are weighted by the local square root of the density in order to be consistent with the semilocal scaling framework and normalized by their maxima. Overall, cases with similar $\mathrm{Re}^\star_\tau$ have similar optimal velocity profiles $\sqrt{\rho}u_{\mathrm{opt}}$ and $\sqrt{\rho}v_{\mathrm{opt}}$. The wall-normal location of the maximum velocity peaks only weakly depends on properties and occurs at $y^\star \approx 8$–10 for u and at $y^\star \approx 12$–14 for v, similar to observations by Pujals *et al.* [11].

V. CRITICAL CONDITIONS FOR SECONDARY INSTABILITY

In this section we aim to explain the modified stability of buffer layer streaks in the case of a nonconstant semilocal Reynolds number across the channel, which was assessed in Sec. II in terms of the modulated intensity of ejection events (see Fig. 3). Hence, we investigate thresholds for the onset of secondary instabilities of the linear optimal streaks. Motivated by the similar characteristics displayed by optimal streaks for cases with similar semilocal Reynolds number discussed in Sec. IV, we now restrict our analysis to constant density flows only, namely, to the cases CP, LL, and SRe$^\star_\tau$GL (see Table I).

The equations governing the evolution of small perturbations to a streamwise-independent two-dimensional base flow $\mathcal{U} = \mathcal{U}(y,z)$ are

$$-i\omega\nabla^2 v + \mathcal{U}\nabla^2 v_x + \mathcal{U}_{zz}v_x + 2\mathcal{U}_z v_{xz} - \mathcal{U}_{yy}v_x - 2\mathcal{U}_z w_{xy} - 2\mathcal{U}_{yz}w_x$$
$$= \frac{1}{\mathrm{Re}}[\mu_e\nabla^4 v + 2\mu_e'\nabla^2 v_y + \mu_e''(v_{yy} - v_{xx} - v_{zz})], \tag{16}$$

$$-i\omega\eta + \mathcal{U}\eta_x - \mathcal{U}_z v_y + \mathcal{U}_{yz}v + \mathcal{U}_y v_z + \mathcal{U}_{zz}w = \frac{1}{\mathrm{Re}}[\mu_e\nabla^2\eta + \mu_e'\eta_y], \tag{17}$$

where the centerline velocity has been used as the reference and the subscripts indicate partial derivatives with respect to the spatial coordinates. Note that the left-hand sides of Eqs. (16) and (17) are the same as for a constant property flow [1] and that the right-hand sides are the same as Eqs. (10) and (11). The viscosity is given by Eq. (2). The reference base flow is the sum of the turbulent mean velocity profile and the nonlinearly saturated optimal streaks. Linear optimal perturbations at β_{opt} with finite amplitudes were advanced in time using a fully nonlinear DNS code until the flow reached the maximum perturbation kinetic energy. We performed simulations using the spectral code SIMSON [38], keeping a fixed base flow (the mean turbulent velocity profile) and advancing the perturbation field only with an imposed eddy viscosity profile on a $\pi \times 2 \times 2\pi/\beta_{\mathrm{opt}}$ box discretized with $48 \times 151 \times 48$ Fourier-Chebyshev-Fourier modes (see [39] for further details on the DNS setup). The two-dimensional flow field corresponding to the time at which the energy amplification of the initial perturbation is largest is used as the condition about which Eqs. (16) and (17) are linearized. The base flow is decomposed into its Fourier modes as

$$\mathcal{U}(y,z) = \mathrm{Re}\left\{\mathcal{U}_0 + 2\sum_{k=1}^{24}\mathcal{U}_k(y)e^{ik\beta z}\right\}. \tag{18}$$

The wall-normal velocity and vorticity have the general form

$$v(x,y,z) = \sum_{k_1=-m}^{m}\tilde{v}_{k_1}(y,t)e^{(ik_1\beta+\gamma)z+i\alpha x-i\omega t}, \tag{19}$$

$$\eta(x,y,z) = \sum_{k_1=-m}^{m}\tilde{\eta}_{k_1}(y,t)e^{(ik_1\beta+\gamma)z+i\alpha x-i\omega t}, \tag{20}$$

with γ the Floquet detuning constant, $\omega = \omega_r + \omega_i i$ the complex eigenvalue, and the spanwise wave number taken as the one corresponding to the optimal streaks calculated in Sec. IV, $\beta = \beta_{\mathrm{opt}}$. We used $N_{\mathrm{mod}} = 151$ Chebyshev modes in the wall-normal direction and $m = 8$ for the expansion of the secondary modes. The effect of increasing this number is negligible on the results. We restrict our attention to the fundamental mode of instability, $\gamma = 0$. We have numerically verified that, for a given set of parameters ($\mathrm{Re}_\tau^\star$, α, and β), increasing γ dampens the critical eigenvalue, hence $\gamma = 0$ provides the most relevant threshold for secondary instability.

In Table III we report the critical parameters for the onset of the secondary instability, namely, the streak amplitude $A = [\max(u) - \min(u)]/[2\max(U)]$, the maximum wall-normal vorticity in semilocal units $\Omega_y^\star = \max_{y,z}(\partial u^+/\partial z^\star)$, the streamwise wave number α, the streamwise wavelength in semilocal and wall units $\lambda_x^\star$ (using $\mathrm{Re}_\tau^\star$ at $y^\star = 12$) and λ_x^+, and the phase velocity of the critical mode of instability $c^+ = (\omega_{r,\mathrm{cr}}/\alpha_{\mathrm{cr}})/u_\tau$. Figure 8 depicts the imaginary part of the eigenvalue that is first destabilized as a function of the streamwise wavelength. Results are shown for the CP, 550CP, 950CP, LL, and $\mathrm{SRe}_\tau^\star$GL cases.

Inspection of Table III reveals that the critical streak amplitude for secondary instability is not significantly affected by property gradients across the channel. Differences with respect to the constant property case at the same friction Reynolds number are small, -1.35% for $\mathrm{SRe}_\tau^\star$GL and $+1.87\%$ for $\mathrm{SRe}_\tau^\star$LL, while the critical streak amplitude for 550CP and 950CP drops by -3.8%

TABLE III. Critical quantities for the secondary instability: streaks amplitude A, maximum local wall-normal vorticity $\Omega_y^\star$, streamwise wave number α, streamwise wavelength in semilocal and wall units $\lambda_x^\star$ and λ_x^+, and phase velocity $c_{\rm cr}^+ = (\omega_{r,\rm cr}/\alpha_{\rm cr})/u_\tau$.

Case	$A_{\rm cr}$	$\Omega_{y,\rm cr}^\star$	$\alpha_{\rm cr}$	$\lambda_{x,\rm cr}^\star$	$\lambda_{x,\rm cr}^+$	$c_{\rm cr}^+$
CP	28.91	0.5359	10.91	228	228	9.49
550CP	27.81	0.5365	15.24	227	227	9.46
950CP	25.77	0.5435	27.14	220	220	9.41
SRe$_\tau^\star$GL	28.52	0.6027	5.61	221	443	12.17
LL	29.45	0.4938	13.78	237	180	8.75

and -10.9%, respectively. On the other hand, the maximum value of local wall-normal vorticity $\Omega_y^\star$ changes considerably for the variable property cases with Re$_\tau^\star$ gradients. This quantity is an indication of the spanwise shear and deformation of the two-dimensional base flow. At a comparable streak amplitude, less wall-normal vorticity is needed to destabilize the streaks if Re$_\tau^\star$ increases away from the walls. The opposite occurs in the case in which Re$_\tau^\star$ decreases. Compared to case CP, $\Omega_{y,cr}^\star$ reduces by -7.9% for the case LL and increases by $+12.5\%$ for the case SRe$_\tau^\star$GL, while it is nearly unchanged for constant property flows at higher Reynolds number (differences are less than 1.5%). The mechanism responsible for changes in the wall-normal vorticity can be discussed in light of the results presented in Sec. IV. The analysis of the growth function showed that the streamwise spacing of optimal streaks $\lambda_z^\star$ is approximately the same, while streaks exhibit a smaller perturbation kinetic energy amplification if Re$_\tau^\star$ increases away from the walls. The result is a weaker streamwise perturbation velocity component for saturated streaks that naturally reduces the spanwise shear $\partial u^+/\partial z^\star$, and in turn the wall-normal vorticity, of the inflectional two-dimensional

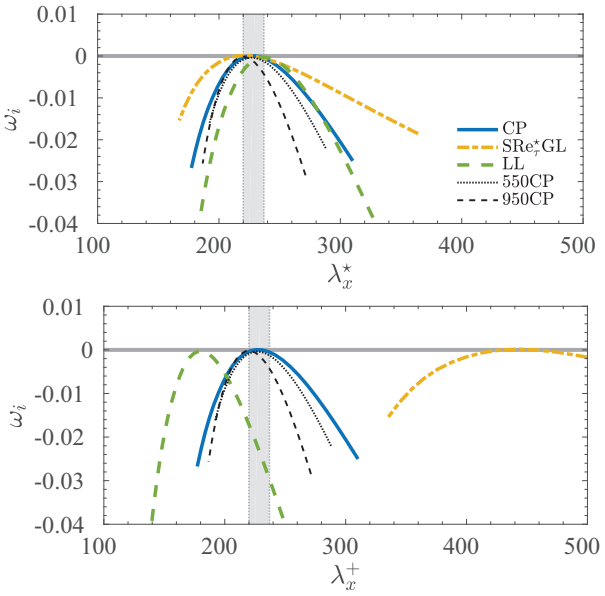

FIG. 8. Streamwise wavelength dependence of the imaginary part of the critical mode of secondary instability. Lengths are expressed in semilocal units using the reference Re$_\tau^\star$ at $y^\star = 12$ (top) and in classical inner units (bottom). The critical conditions reported in Table III correspond to the maximum of each curve. The shaded area indicates the range of values encompassing $\lambda_{x,\rm cr}^\star$ for all cases considered.

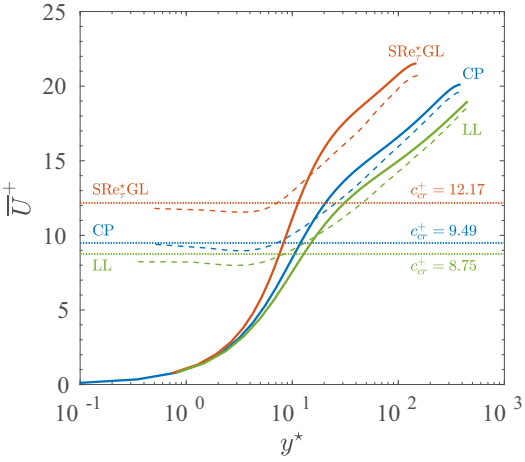

FIG. 9. Wall-normal profiles of mean turbulent velocity $\overline{U}^+$ (solid) and of streamwise convection velocity C_u^+ (dashed) in wall units. Here C_u^+ is defined as in [43]. The horizontal dotted lines indicate the phase velocity of the critical mode.

velocity profile $\mathcal{U}(y,z)$ that undergoes the instability. Similar reasoning can be used to analyze the cases with decreasing $\mathrm{Re}_\tau^\star$ away from the walls. This modulating effect can be interpreted in relation to the discussion of the modified ejection events of Sec. II (see Fig. 3), which become stronger for the turbulent flow cases LL and $\mathrm{SRe}_\tau^\star$LL compared to CP and weaker for GL and $\mathrm{SRe}_\tau^\star$GL. Patel *et al.*[33] showed that the root-mean-square vorticity fluctuations in turbulent channels with variable properties scale in semilocal units, $(\hat{\omega}_y^\star)_{\mathrm{rms}}$, such that flows with constant, liquidlike, and gaslike behavior of $\mathrm{Re}_\tau^\star$ are characterized by similar profiles of $(\hat{\omega}_y^\star)_{\mathrm{rms}}$ between $y^\star = 9$ and $y^\star = 100$. The consequence of having similar levels of wall-normal vorticity and a lower critical threshold for the case LL, compared to CP, is the occurrence of stronger bursts of the streaks. The opposite mechanism motivates the weaker ejections observed for GL and $\mathrm{SRe}_\tau^\star$GL.

The critical wavelength of the secondary mode scales in semilocal units and attains values $\lambda_{x,\mathrm{cr}}^\star \approx 220$–$237$ for all cases considered. This critical value is consistent with relevant characteristic lengths previously found by other authors studying fully turbulent flows. From a physical point of view, secondary instabilities of streaks are strongly connected to the generation of wall-normal velocity fluctuations and to quasistreamwise vortices that modulate the streaks streamwise oscillations. Jiménez *et al.* [40] showed that in the near-wall region most of the spectrum of the vertical velocity is concentrated into structures of length $\lambda_x^+ \approx 300$. Further investigation of vortex clustering in the logarithmic region of turbulent channels [41] provided a lower limit for the centerline of the attached clusters to $y^+ \approx 25$, whose streamwise extent is $\lambda_x^+ \approx 200$. The value of $\lambda_{x,\mathrm{cr}}^\star$ calculated here is closely related to the minimum box size needed for instabilities to develop and to have sustained turbulence, $L_{x,\mathrm{min}}^+ \approx 250$–$350$ [42].

Interestingly, we find that the critical mode of secondary instability provides a reasonably good estimate of the convection speed of the flow in the near-wall region. Figure 9 shows the mean streamwise velocity profiles for cases CP, LL, and $\mathrm{SRe}_\tau^\star$GL together with their convection speeds calculated following the procedure of del Álamo and Jiménez [43]. Horizontal lines indicate the phase velocity of the critical mode calculated by the linearized theory, whose values are summarized in Table III. In the logarithmic region, the convection velocity follows the mean velocity, while its profile departs from the latter and flattens out near the wall ($y^\star < 10$). The constant value approached in this region is closely approximated by the phase velocity of the critical mode, suggesting that most of the coherent streamwise propagation of information is captured by the instability mode. Notably, our linearized approach additionally captures the modulating effect of variable viscosity that result in respectively higher and lower convection speed if $\mathrm{Re}_\tau^\star$ decreases or increases away from the walls.

VI. CONCLUSION

We have used the framework of the linearized Navier-Stokes equations to investigate the stability of turbulent flows in channels with temperature-dependent density and viscosity. Mean profiles of fluid properties and eddy viscosity were taken from DNSs [32] and used to calculate the effective viscosity coefficient and the base velocity profile from the one-dimensional momentum balance, adopting the same methodology as previous studies, e.g., [10,11]. We have shown that the semilocal scaling not only applies to the analysis of fully turbulent flows, but additionally provides an effective parametrization of the effect of variable properties on optimal streaks and their critical mode of secondary instability calculated using the linear theory. We also presented linear stability results that serve as arguments to explain the modulating effect of temperature-dependent properties on the intensity and stability of buffer layer streaks observed in DNSs.

A transient growth analysis on the mean turbulent profiles has shown that optimal streaks corresponding to the inner peak of the growth function scale in semilocal units to an approximately constant wavelength $\lambda^\star_{z,\mathrm{opt}} \approx 90$ for both constant and variable property cases. Furthermore, flow cases with different property distributions, but similar semilocal Reynolds number $\mathrm{Re}^\star_\tau$, display a collapse of their growth function at small scales $\lambda^\star_z < 300$ and of their optimal velocity profiles expressed in semilocal distance from the wall. The modulating effect of increasing or decreasing $\mathrm{Re}^\star_\tau$ across the channel appears in a modification of the maximum growth attained by the optimal streaks. In contrast to flows with constant $\mathrm{Re}^\star_\tau$ profiles, for which the value of the growth function corresponding to the inner peak is independent of Re_τ, the energy amplification is reduced if $\mathrm{Re}^\star_\tau$ increases away from the wall, while it increases if $\mathrm{Re}^\star_\tau$ decreases away from the wall. This is consistent with the modulation of the strength of buffer layer streaks observed in DNSs.

An investigation of the stability of a two-dimensional base flow consisting of the turbulent mean velocity profile and the perturbation field of nonlinearly saturated optimal streaks of finite amplitude has revealed that the critical wavelength of streamwise instability scales in semilocal units to $\lambda^\star_x \approx 230$ for all cases considered. We quantified the effect of nonuniform $\mathrm{Re}^\star_\tau$ caused by variable viscosity on the critical threshold of base flow deformation in order to trigger secondary instability. If $\mathrm{Re}^\star_\tau$ increases away from the walls, the threshold of spanwise shear deformation is significantly lower than the value for constant property flows in the range $\mathrm{Re}_\tau = 395$–950, which is approximately constant. In view of this modified threshold, buffer layer streaks in a turbulent channel with increasing semilocal Reynolds number towards the centerline can be regarded as less stable, thus explaining the more intense ejection events observed in DNSs of such flows. Opposite conclusions are drawn for a decreasing distribution of $\mathrm{Re}^\star_\tau$. Finally, we have shown that the phase velocity of the critical mode of secondary instability provides a good estimate of the convection velocity in the near-wall region for both constant and variable viscosity cases.

ACKNOWLEDGMENTS

The authors thankfully acknowledge Ardeshir Hanifi for providing the secondary stability code used in Sec. V. E.R. gratefully acknowledges financial support from the Linné FLOW Centre and Shervin Bagheri for fruitful discussions and for providing comments on a draft of the paper. Computational resources were provided by the Swedish National Infrastructure for Computing at HPC2N (Abisko).

[1] P. J. Schmid and D. S. Henningson, *Stability and Transition Shear Flows*, edited by J. E. Marsden and L. Sirovich (Springer, Berlin, 2001).

[2] J. M. Hamilton, J. Kim, and F. Waleffe, Regeneration mechanisms of near-wall turbulence structures, J. Fluid Mech. **287**, 317 (1995).

[3] J. Jiménez and A. Pinelli, The autonomous cycle of near-wall turbulence, J. Fluid Mech. **389**, 335 (1999).
[4] L. Brandt, The lift-up effect: The linear mechanism behind transition and turbulence in shear flows, Eur. J. Mech. B **47**, 80 (2014).
[5] H. L. Gustavsson, Energy growth of three-dimensional disturbances in plane Poiseuille flow, J. Fluid Mech. **224**, 241 (1991).
[6] S. C. Reddy, P. J. Schmid, and D. S. Henningson, Pseudospectra of the Orr-Sommerfeld operator, SIAM J. Appl. Math. **53**, 15 (1993).
[7] L. N. Trefethen, A. E. Trefethen, S. C. Reddy, and T. A. Driscoll, Hydrodynamic stability without eigenvalues, Science **261**, 578 (1993).
[8] K. M. Butler and B. F. Farrell, Optimal perturbations and streak spacing in wall-bounded turbulent shear flow, Phys. Fluids **5**, 774 (1993).
[9] C. R. Smith and S. P. Metzler, The characteristics of low-speed streaks in the near-wall region of a turbulent boundary layer, J. Fluid Mech. **129**, 27 (1983).
[10] J. C. del Álamo and J. Jiménez, Linear energy amplification in turbulent channels, J. Fluid Mech. **559**, 205 (2006).
[11] G. Pujals, M. Garcia-Villalba, C. Cossu, and S. Depardon, A note on optimal transient growth in turbulent channel flows, Phys. Fluids **21**, 015109 (2009).
[12] R. D. Cess, A survey of the literature on heat transfer in turbulent tube flow, Westinghouse No. 8-0529-R24, 1958 (unpublished).
[13] W. C. Reynolds and A. K. M. F. Hussain, The mechanics of an organized wave in turbulent shear flow. Part 3. Theoretical models and comparisons with experiments, J. Fluid Mech. **54**, 263 (1972).
[14] E. Kim, H. Choi, and J. Kim, Optimal disturbances in the near-wall region of turbulent channel flows, Phys. Rev. Fluids **1**, 074403 (2016).
[15] W. Schoppa and F. Hussain, Coherent structure generation in near-wall turbulence, J. Fluid Mech. **453**, 57 (2002).
[16] J. Jiménez, How linear is wall-bounded turbulence? Phys. Fluids **25**, 110814 (2013).
[17] J. Jiménez, Direct detection of linearized bursts in turbulence, Phys. Fluids **27**, 065102 (2015).
[18] C. Cossu, G. Pujals, and S. Depardon, Optimal transient growth and very large-scale structures in turbulent boundary layers, J. Fluid Mech. **619**, 79 (2009).
[19] J. Park, Y. Hwang, and C. Cossu, On the stability of large-scale streaks in turbulent Couette and Poiseuille flows, C. R. Mec. **339**, 1 (2011).
[20] F. Alizard, Linear stability of optimal streaks in the log-layer of turbulent channel flows, Phys. Fluids **27**, 105103 (2015).
[21] A. A. Townsend, *The Structure of Turbulent Shear Flow* (Cambridge University Press, Cambridge, 1976).
[22] M. Marquillie, U. Ehrenstein, and J.-P. Laval, Instability of streaks in wall turbulence with adverse pressure gradient, J. Fluid Mech. **681**, 205 (2011).
[23] F. Alizard, S. Pirozzoli, M. Bernardini, and F. Grasso, Optimal transient growth in compressible turbulent boundary layers, J. Fluid Mech. **770**, 124 (2015).
[24] G. Brethouwer, P. Schlatter, Y. Duguet, D. S. Henningson, and A. V. Johansson, Recurrent Bursts via Linear Processes in Turbulent Environments, Phys. Rev. Lett. **112**, 144502 (2014).
[25] G. Brethouwer, Linear instabilities and recurring bursts of turbulence in rotating channel flow simulations, Phys. Rev. Fluids **1**, 054404 (2016).
[26] G. N. Coleman, J. Kim, and R. D. Moser, A numerical study of turbulent supersonic isothermal-wall channel flow, J. Fluid Mech. **305**, 159 (1995).
[27] L. Duan, I. Beekman, and M. P. Martín, Direct numerical simulation of hypersonic turbulent boundary layers. Part 2. Effect of wall temperature, J. Fluid Mech. **655**, 419 (2010).
[28] M. Lagha, J. Kim, J. D. Eldredge, and X. Zhong, A numerical study of compressible turbulent boundary layers, Phys. Fluids **23**, 015106 (2011).
[29] P. G. Huang, G. N. Coleman, and P. Bradshaw, Compressible turbulent channel flows: DNS results and modelling, J. Fluid Mech. **305**, 185 (1995).
[30] Y. Morinishi, S. Tamano, and K. Nakabayashi, Direct numerical simulation of compressible turbulent channel flow between adiabatic and isothermal walls, J. Fluid Mech. **502**, 273 (2004).

[31] H. Foysi, S. Sarkar, and R. Friedrich, Compressibility effects and turbulence scalings in supersonic channel flow, J. Fluid Mech. **509**, 207 (2004).
[32] A. Patel, J. W. R. Peeters, B. J. Boersma, and R. Pecnik, Semi-local scaling and turbulence modulation in variable property turbulent channel flows, Phys. Fluids **27**, 095101 (2015).
[33] A. Patel, B. J. Boersma, and R. Pecnik, The influence of near-wall density and viscosity gradients on turbulence in channel flows, J. Fluid Mech. **809**, 793 (2016).
[34] A. Trettel and J. Larsson, Mean velocity scaling for compressible wall turbulence with heat transfer, Phys. Fluids **28**, 026102 (2016).
[35] H. Nemati, A. Patel, B. J. Boersma, and R. Pecnik, Mean statistics of a heated turbulent pipe flow at supercritical pressure, Int. J. Heat Mass Transfer **83**, 741 (2015).
[36] S. C. Reddy and D. S. Henningson, Energy growth in viscous channel flows, J. Fluid Mech. **252**, 209 (1993).
[37] S. Hoyas and J. Jiménez, Reynolds number effects on the Reynolds-stress budgets in turbulent channels, Phys. Fluids **20**, 101511 (2008).
[38] M. Chevalier, P. Schlatter, A. Lundbladh, and D. S. Henningson, SIMSON: A pseudo-spectral solver for incompressible boundary layer flows, KTH Mechanics, Stockholm, Sweden, 2007, Tech. Rep., TRITA-MECH 2007:07.
[39] G. Eitel-Amor, R. Örlü, P. Schlatter, and O. Flores, Hairpin vortices in turbulent boundary layers, Phys. Fluids **27**, 025108 (2015).
[40] J. Jiménez, J. C. del Álamo, and O. Flores, The large-scale dynamics of near-wall turbulence, J. Fluid Mech. **505**, 179 (2004).
[41] J. C. del Álamo, J. Jiménez, P. Zandonade, and R. D. Moser, Self-similar vortex clusters in the turbulent logarithmic region, J. Fluid Mech. **561**, 329 (2006).
[42] J. Jiménez and P. Moin, The minimal flow unit in near-wall turbulence, J. Fluid Mech. **225**, 213 (1991).
[43] J. C. del Álamo and J. Jiménez, Estimation of turbulent convection velocities and corrections to Taylor's approximation, J. Fluid Mech. **640**, 5 (2009).